Assessment of the LES-FGM framework for capturing stable and unstable modes in a hydrogen / methane fuelled premixed combustor

J. Z. Ho[a,*], S. Jella[b], M. Talei[a], G. Bourque[b], T. Indlekofer[c], J. Dawson[d]

[a]*Department of Mechanical Engineering, University of Melbourne, Parkville, VIC 3010, Australia*
[b]*Siemens Canada Limited, Montreal, QC H9P 1A5, Canada*
[c]*SINTEF Energy Research, Trondheim 7034, Norway*
[d]*Department of Energy and Process Engineering, Norwegian University of Science and Technology, Trondheim N-7491, Norway*

Abstract

The main objective of this paper is to assess the capability of compressible Large Eddy Simulations (LES) to capture azimuthal combustion instability. The thickened flame model coupled with Flamelet Generated Manifold (FGM) tabulated chemistry is used as the combustion model. LES of an annular combustor is performed for five cases featuring stable and unstable combustion of hydrogen-methane mixtures. The unstable modes feature azimuthal instabilities and this annular combustor is used to test the LES-FGM framework. A consistent methodology is applied across all cases. It is found that LES predicts azimuthal modes for stable cases but these modes are weak and intermittent with pressure fluctuation amplitudes within the order of experimental noise. In addition, the unstable cases capture azimuthal modes that have approximately the same frequency as that of the experiment though

---

[*]Corresponding author:
   Email address: `jenzen.ho@unimelb.edu.au` (J. Z. Ho)

the amplitudes of the modes are over-predicted. This suggests that the de-scribed LES-FGM framework is able to predict the onset of thermoacoustic instabilities and their qualitative changes with addition of hydrogen.

Keywords:

Thermoacoustic instability, Hydrogen, Methane, LES

---

1. Introduction

Stationary gas turbines are an important form of dispatchable power generation that can complement intermittent renewable energy sources and therefore provide stability for the electrical grid. These gas turbines domi-nantly burn natural gas but with emerging fuels such as hydrogen, they can be decarbonised and provide both base-load and peak-load power. Although adding hydrogen to natural gas, which primarily consists of methane, can lead to desirable properties such as a wider flammability range, it introduces significant challenges. Flashback is more likely to occur [1], and the sound generated from flame annihilation of these fuel blends can feature very large wavelengths due to the high diffusivity of hydrogen, which was a feature not found in pure hydrogen or methane flames [2]. Furthermore, the increase in the laminar [3, 4] and turbulent [5] flame speed can trigger thermoacoustic instability in otherwise stable systems [6, 7].

Thermoacoustic instability is characterised by large pressure oscillations that are generated from the coupling of the flame, flow and acoustic modes of the combustor. These oscillations can damage the combustor if they are strong enough, and they are generally detected only in the late stages of the design process, which makes them expensive to fix [8, 9]. Thermoacoustic in-

2

stabilities in annular combustors commonly feature azimuthal modes. These modes are sustained through a coupling of flow dynamics with acoustics generated by the flame [10–12], but can also be influenced by the interaction between neighbouring burners [13]. A review of the literature shows that a large number of experimental studies have focused on model combustors with single burners whereas annular combustors, which are commonly present in gas turbines, are less frequently studied. This is primarily because an annular burner featuring 10-20 burners in the same chamber is an expensive setup and the analysis of the flames is also difficult due to the complexity involved [13].

There are multiple numerical tools such as Large Eddy Simulations (LES) and low-order models that make use of Flame Transfer Functions (FTF) [14], which is a measure of the heat release rate response to velocity fluctuations, to model the flame response. They can be very useful to predict thermoacoustic instability induced by azimuthal modes. LES has several advantages compared to low-order modeling approaches which require prior knowledge or simplifying assumptions regarding the response of the flame to velocity fluctuations. As such, low-order models are not able to capture transient interactions between injectors such as the propagation of flame from one injector to another during ignition, and they cannot take into account the effect of interacting flames between adjacent injectors in an annular chamber [15, 16]. However, LES can capture details such as light-round of an annular chamber [17] and reveal how they can influence different instability modes. The earliest LES studies were undertaken by the combustion group at CERFACS [18–20]. The code AVBP developed at CERFACS was

used to simulate different cases with the Thickened Flame Modelling (TFM) approach combined with single- or two-step chemistry.

Multiple LES studies were conducted to simulate an annular combustor of a helicopter engine by CERFACS [16, 21]. Their simulations captured limit cycle oscillations of azimuthal modes with different amplitudes when two variants of the swirler configuration were used, demonstrating that LES is capable of capturing differences in the limit cycle amplitudes [22]. In addition, they were able to show that the azimuthal instabilities continued to exhibit the same frequencies after switching from a coarse mesh to a finer mesh [23].

Following on from the success of capturing azimuthal instabilities, the same group simulated a 15° sector of a full gas turbine injector [18]. They found that simulating the mixing between fuel and air in the plenum upstream of the injectors was necessary in order to capture the effect of equivalence ratio oscillations on the heat release rate fluctuations. To extract the correct FTF the pulsating injected fuel flow rate and the fluctuating trajectory of the fuel jets needed to be captured. The full gas turbine was then simulated and the mean flow field was validated against cold flow experiments [19]. They obtained the FTFs of two stable conditions, one with the flame attached to the bluff body and one with the flame detached from the bluff body. The FTFs predicted a higher amplitude response at high frequencies for the detached flame than the attached one, suggesting that thermoacoustic instability may be triggered differently in those conditions.

Lab scale annular combustors have also been simulated by other groups using different combustion models. Tachibana *et al.* [24] used a flamelet

4

and progress variable combustion model to simulate their annular combustor fuelled by a liquid mixture of dodecane, iso-octane and toluene. Their LES predicted a pressure oscillation amplitude of about half of that observed in the experiment at the dominant peak frequency which was also slightly higher than the experiment. They suggested that the reason for the discrepancies is related to the modelling of the spray atomisation process, which has a large uncertainty. Zettervall *et al.* [25] simulated Dawson and Worth's [26] atmospheric annular combustor fuelled by methane and ethylene using finite rate chemistry with the Partially Stirred Reactor (PaSR) combustion model. They were able to show that qualitatively the LES flame shapes matched those of the experiments. The ethylene case reproduced a peak frequency at 1715 Hz compared to the experimental data of 1720 Hz. However, there were significant pressure fluctuations at other frequencies not found in the experiment. In addition, the methane case found a weak azimuthal mode at 1698 Hz and a strong longitudinal mode at 924 Hz, showing that both longitudinal and azimuthal modes can exist simultaneously in the burner. In fact, all atmospheric modes found were coupled azimuthal and longitudinal modes as first shown by the atmospheric annular combustor experiments in EM2C [27, 28]. The occurrence of the coupled mode was also found by Chen *et al.* [29] who simulated Dawson and Worth's [26] atmospheric annular combustor. Their LES was able to detect azimuthal modes, though the frequency was overpredicted by 100-150 Hz and the amplitude was underpredicted by 5-8%. In addition, there were peaks in frequencies lower than the fundamental azimuthal frequency that was not observed by experiments. The simulation did not include the upstream conical inlet volume, and by us-

ing low-order modelling and modifying the effective inlet length of this model it was found that this omission was the main reason for the overprediction of the fundamental frequency of the azimuthal mode. They also observed that the initialisation can have a significant effect on the development of azimuthal modes. It takes the simulation approximately 0.1 s longer to transition from longitudinal mode to azimuthal mode when igniting the entire annular chamber simultaneously compared to only igniting a single point.

To the authors' knowledge, no LES study has simulated the effect of hydrogen addition to methane on azimuthal modes at elevated pressures. The experimental study by Indlekofer *et al.* [30] showed that a pressurised annular combustor can be completely stable with pure methane for a wide range of operating conditions but addition of 25% H_2 by volume can trigger thermoacoustic instabilities. This effect was not observed in the atmospheric version of the combustor [26, 31]. In addition, when thermoacoustic modes are triggered, the amplitude of these modes are non-linearly dependent on the amount of hydrogen. The mode amplitude at 25% hydrogen by volume is larger than at 43% hydrogen by volume. High speed imaging of OH* chemiluminescence revealed that the heat release rate response of a higher hydrogen content case is out of phase with the pressure oscillations, which results in an overall lower amplitude [32].

It is important that LES is able to accurately predict the dependence of the thermoacoustic modes on the level of hydrogen addition. All the LES studies discussed have focused on simulating only unstable azimuthal modes. However, it is also important that stable cases are also captured by LES. A consistent methodology that employs relatively cheap LES models

is required so that the onset and severity of thermoacoustic modes can be predicted accurately for many different operating conditions. To this end, LES-FGM is tested instead of relatively more expensive LES models such as finite rate chemistry.

The aim of this study is to assess the capability of this framework in capturing the transition from stable to unstable combustion and also azimuthal modes in unstable cases for the annular burner used by the Norwegian University of Science and Technology (NTNU) [30, 33]. Specifically, the Intermediate Pressurised Annular (IPA) combustor of Indlekofer *et al.* [30] fuelled with various hydrogen and methane mixtures will be simulated. This combustor is chosen because it is the first pressurised annular burner that investigates the effect of hydrogen content, and it has well characterised boundary conditions which reduces the assumptions required for the simulation. A consistent methodology is developed and tested on both thermoacoustically stable and unstable cases. Five test conditions, two of which are thermoacoustically unstable and three of which are thermoacoustically stable, are simulated. A coarser and a finer mesh are considered for one of the unstable conditions to examine the effect of the mesh on the results.

2. Methodology

StarCCM+ [34] was used to perform LES of the annular combustor used in [30, 33]. Chemistry was tabulated using the FGM method [35, 36] and modelled using TFM [37]. The flamelets were generated using the Freely Propagating Flame (FPF) solutions in the progress variable space. The flamelet equations in the progress variable space, solving for the gradient

of the unnormalised progress variable, $g_c = \partial Y_c / \partial x$, mass fraction of species k, Y_k, and temperature, T, are written as per Scholtissek $et\ al.$ [38]:

$$
\begin{aligned}
0 = & \frac{g_c}{c_p} \frac{\partial}{\partial Y_c} \left(g_c \lambda \frac{\partial T}{\partial Y_c} \right) + g_c \frac{\partial}{\partial Y_c} (g_c \rho Y_c \tilde{V}_c) \frac{\partial T}{\partial Y_c} \\
& + g_c^2 \sum_k \frac{c_{p,k}}{c_p} \rho Y_k \tilde{V}_k \frac{\partial T}{\partial Y_c} - \dot{\omega}_c \frac{\partial T}{\partial Y_c} + \frac{\dot{\omega}_T}{c_p},
\end{aligned}
\tag{1}
$$

$$
0 = - g_c \frac{\partial}{\partial Y_c} (g_c \rho Y_i \tilde{V}_i) + g_c \frac{\partial}{\partial Y_c} (g_c \rho Y_c \tilde{V}_c) \frac{\partial Y_i}{\partial Y_c} - \dot{\omega}_c \frac{\partial Y_i}{\partial Y_c} + \dot{\omega}_i,
\tag{2}
$$

$$
0 = - g_c^2 \frac{\partial^2}{\partial Y_c^2} (g_c \rho Y_c \tilde{V}_c) - \dot{\omega}_c \frac{\partial g_c}{\partial Y_c} + g_c \frac{\partial \dot{\omega}_c}{\partial Y_c},
\tag{3}
$$

where the unnormalised progress variable, $Y_c = \sum_k \alpha_k Y_k$, α_k is a weighting factor and Y_k is the mass fraction of species k, c_p is the specific heat capacity, $c_{p,k}$ is the specific heat capacity of species k, ρ is the density, $\tilde{V}_k$ is the diffusion velocity in the progress variable space and is solved using the mixture-averaged diffusion formulation [39], and $\dot{\omega}_c$, $\dot{\omega}_T$ and $\dot{\omega}_i$ are the chemical source terms for the normalised progress variable, temperature and species respectively.

The thickening factor, F, for the TFM takes the form:

$$
F = 1 + (F_l - 1)S,
\tag{4}
$$

$$
F_l = \min(F_{\max}, \frac{N \Delta_x}{\delta}),
\tag{5}
$$

where $F_{\max} = 20$, $N = 3$, Δ_x is the grid size, and the flame thickness is set to the 1D FPF thermal flame thickness, $\delta = \delta_{th} = (T_u - T_b)/\max(\frac{dT}{dx})$.

Heat losses are taken into account by reducing the total enthalpy of the flamelets as per Donini $et\ al.$ [40]. A heat loss ratio, $r_h = (h_{ad} - h)/h_s$, where

h_{ad} is the adiabatic total enthalpy of a FPF unaffected by heat losses, and h_s is the sensible enthalpy, is firstly defined. Flamelets are then calculated for 11 flamelets with r_h between -3 and 3 by setting the inlet temperature of a flamelet affected by heat losses with total enthalpy, h.

The efficiency function proposed by Charlette *et al.* [41] was used. For brevity, the efficiency function will not be redefined here but the model constants will be reported. The model exponent, $b = 1.4$, and the Kolmogorov constant, $C_k = 1.5$, were used as per their suggested values. The model exponent, $\beta = 0.5$ was used.

The flame sensor for TFM, S, is defined as

$$S = \tanh \left(\beta_S \frac{Y_{CH_2O}Y_{OH}}{\max(Y_{CH_2O}Y_{OH})} \right) \left(\frac{Y_{OH}}{\max(Y_{OH})} \right)^\alpha, \tag{6}$$

where $\alpha = 1.5$, and $\beta_S = 50$. The maximums are conditioned on the mixture fraction, Z. This form of the sensor with OH weighting to avoid excessive broadening of the thickening envelope has been described previously in [42].

The IPA combustor cases fuelled with hydrogen and methane published by Indlekofer *et al.* [30] was simulated. The details of the experiment can be found in the original paper, and five cases were selected to be simulated in this work. Table 1 shows the five cases, with the three thermoacoustically stable cases named S1–S3, and the two unstable cases named U1 and U2.

Figure 1 shows the geometry of the simulated combustor. In the experiment, a high blockage sintered metal plate was installed a short distance (2 mm) upstream of the inlets to the injectors. In initial simulations, the small distance between the sintered metal plate and the injector inlets was consid-

Table 1: IPA combustor cases. For all cases, air mass flow rate is 91.85 g/s, and $T_u = 293$ K.

Case	ϕ	%H$_2$ by volume in fuel	s_L [m/s]	δ_{th} [μm]
S1	0.8	0	0.20	344
S2	0.65	0	0.10	570
S3	0.65	25	0.124	482
U1	0.8	25	0.24	308
U2	0.8	43	0.29	274

ered but led to unphysical oscillations. Subsequently, in the presented cases the inlets to the injectors were modeled as discrete, fully reflective mass flow inlets. This assumption is also strengthened by the acoustic characterisation of the sintered metal plate [30] which shows that it is strongly reflective. The remaining geometry of the injectors and combustion chamber was recreated using the supplementary material of [30]. Only the converging part of the outlet was considered with a non-reflecting pressure outlet using a characteristic length of 1 m [43]. The wall temperatures were fixed as Dirichlet boundary conditions such that they are equal to the temperatures measured in the experiment.

The progress variable for FGM was optimised for case U1 such that it minimizes the gradients of the tabulated variables with respect to the unnormalised progress variable, Y_c. This procedure yields $Y_c = Y_{CO_2} + Y_{CO} + 0.125Y_{H_2} + 0.125Y_{H_2O}$, which was used for all simulations. A 22-species mechanism named AR22 that has been reduced from AramcoMech [44] was used for the flamelet table generation as this mechanism has been shown to accurately predict the laminar burning velocity of hydrogen and methane mix-
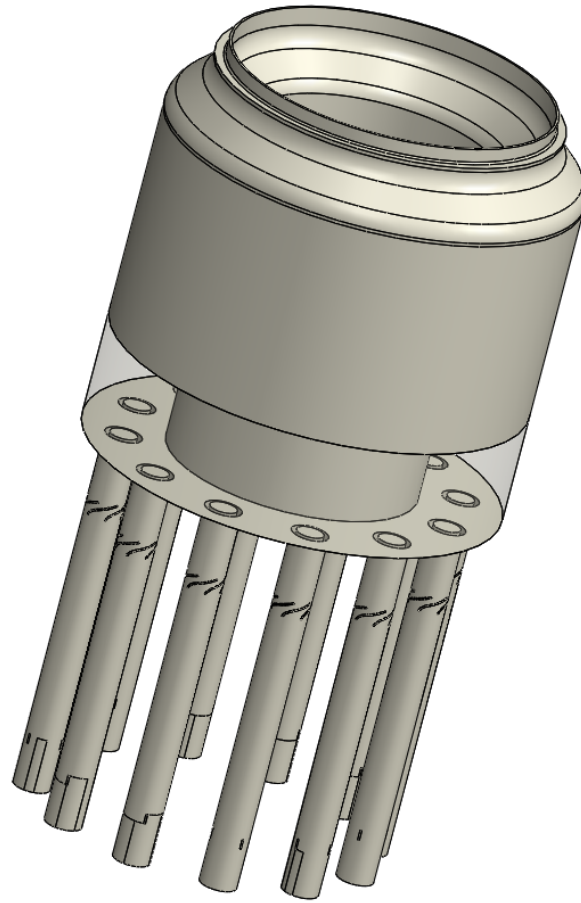
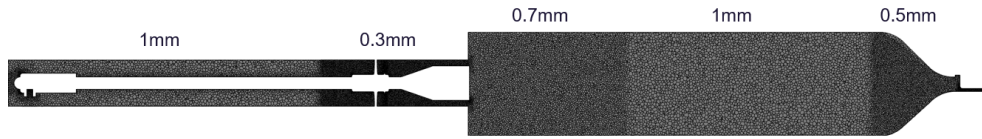Figure 1: Geometry of the simulated domain. The quartz section of the outer wall is transparent.

Figure 2: Partial cross-section of the NTNU combustor showing the mesh size.

tures [45]. The Wall-Adapting Local-Eddy (WALE) viscosity subgrid scale model [46] was used with the model constant related to the length scale, $C_w = 0.544$, the von Karman constant, $\kappa = 0.41$, and $C_t = 3.5$ for all simulations.

Figure 2 shows the mesh size in a cross-section of the NTNU combustor. For all cases, a polyhedral mesh with refinements in the critical areas was used. The mesh was identical for all cases. The injector and post-flame zone have $\Delta_x = 1$ mm, the swirlers have $\Delta_x = 0.3$ mm, the flame zone has $\Delta_x = 0.7$ mm, and the converging section has $\Delta_x = 0.5$ mm.

The simulations were initialised using a Reynolds-Averaged Navier Stokes (RANS) solution. The initial RANS simulation was used to prescribe the outlet pressure such that the mean pressure in the injectors is equal to that of the experimental pressure probes at the same location. After the RANS has converged, LES was run for 100 milliseconds with $\Delta t = 10 \times 10^{-6}$ s with the first-order PISO algorithm for time discretisation. The large timestep and a dissipative numerical scheme were intentionally used as they cause dissipation of the initial numerical waves that occur when switching from RANS to LES. After the initial numerical noise was dissipated in the domain, the time discretisation scheme was switched to a second-order implicit solver with $\Delta t = 5 \times 10^{-6}$ s. This corresponds to a convective CFL, $\text{CFL}_\text{c} < 0.5$

for the flame and flow zones, and $CFL_c \approx 5$ for the converging nozzle. The maximum acoustic CFL, $CFL_{ac} \approx 8$ in the post-flame zone with 1 mm mesh for all cases. The mesh consists of 17.2 million cells, with the simulations of the stable cases costing approximately 10,000 compute-hours each, and the simulations of the unstable cases costing 30,000 compute-hours each as the unstable cases required longer simulation times for a limit cycle to establish and statistical data to be gathered. The simulations were run in parallel with 400 processes on Intel Skylake cores.

To demonstrate the methodology used, Figure 3 shows the pressure trace for a point 175 mm downstream of the injectors in the combustion chamber for Case U1. The initial p value is found from RANS and the solution oscillates around the initial RANS value. The initial noise caused from switching from RANS to LES favours the appearance of axial modes, and must be damped out by the first-order PISO scheme with $\Delta t = 10 \times 10^{-6}$ s. If a strongly dissipative scheme is not used, or if the timestep is too small hence numerical dissipation is small, these initial axial waves grow and generate axial thermoacoustic modes. These axial thermoacoustic modes do not transition into azimuthal modes after running for approximately 0.4 s. This occurs even for the stable cases, hence the first-order PISO scheme with a large timestep is chosen to dissipate the initial numerical noise. The appearance of strong persistent axial modes is contrary to experimental results and is a result of the pressure wave generated by the switch from RANS to LES.

Once the numerical artefacts due to the RANS to LES switchover have dissipated and large coherent structures have been fully developed in the velocity field, the time discretisation scheme was switched to second-order
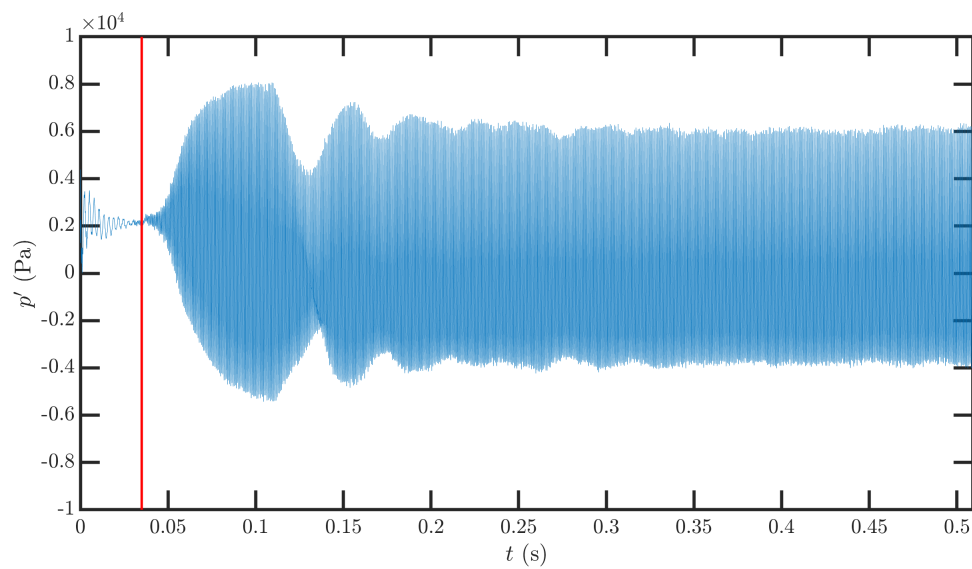
Figure 3: Pressure fluctuations at a point 175 mm downstream of the injectors in the combustion chamber for Case U1. The initial p value is found from RANS, and the red line denotes the switch from first-order PISO with $\Delta t = 10 \times 10^{-6}$ s to second-order implicit with $\Delta t = 5 \times 10^{-6}$ s.

implicit and the time step was reduced. If a case is unstable, it was found
that the pressure waves increase in magnitude as thermoacoustic instability
is triggered. It was also found that large wavelength pressure waves were
developed after thermoacoustic instability is triggered. This large wavelength
pressure wave was found to slowly decrease in amplitude as the simulation
continued. In order to reach a constant limit cycle and eliminate this wave,
the simulations were required to run for ≈ 0.3 s, which is ≈ 14 flowthrough
times.

3. Results

Figure 4 shows the instantaneous flame sensor field for Cases S1, S3, U1,
and U2. The flames appear to be longer for the stable cases and shorter for
the unstable cases. To verify this, the flame lengths are obtained. The flame
lengths, L_f, shown in Table 2, are calculated by finding the location of the
maximum value of the radially-integrated mean heat release rate indicator
for a cross-section through the middle of one of the flames. The heat release
rate indicator is calculated by assuming a 1-step reaction where the fuel is
converted into CO_2 and H_2O, and then calculating the heat of reaction as:

$$h_R = \sum_{Y_k^F} h_k^o - n h_{CO_2}^o - \frac{m}{2} h_{H_2O}^o, \tag{7}$$

where Y_k^F is the mass fraction of the kth species in the fuel, h_k^o is the
formation enthalpy of species k, n is the molar coefficient of CO_2, and $m/2$
is the molar coefficient of H_2O in the stoichiometrically balanced chemical
reaction equation.

Table 2: Flame lengths for Case S3, U1 and U2 for the LES and experimental data [30].

LES/Experiment	S1	S2	S3	U1	U2
LES	21.5	40.5	22.5	14.5	16.0
Experiment	–	–	20.2	17.0	18.6

The larger flame lengths of the stable cases appear to cause the neighbouring flames of two injectors to interact and in some cases merge together in these cases. A shorter and more compact flame for the unstable cases suggest that the flames in these cases have a higher turbulent burning velocity.

The blue circles in Figure 4 show that for the unstable flames, pockets of unburnt reactants are generated. These pockets then burn out and may interact directly with the flame next to it. It is observed that for the unstable flames this occurs regularly at a frequency that is in sync with the fundamental frequency of the azimuthal mode, while the stable flames pockets are stochastically generated and destroyed. This behaviour can be seen in the animation of the heat release rate and pressure fluctuation in the supplementary material 'U1_anim.mp4'.

Figure 5 shows the mean heat release rate indicator from LES for Cases S3, U1 and U2, and also shows the mean OH* chemiluminescence from experimental data [30]. In order to directly compare against experimental chemiluminescence images, which is a line-of-sight method, the mean cross-sectional h_R was rotated $180°$ and then integrated in the direction of the radius of the large annulus.

The flame shapes show good agreement between LES and experimental data. The angle of the flames, the flame lengths, and the location of highest

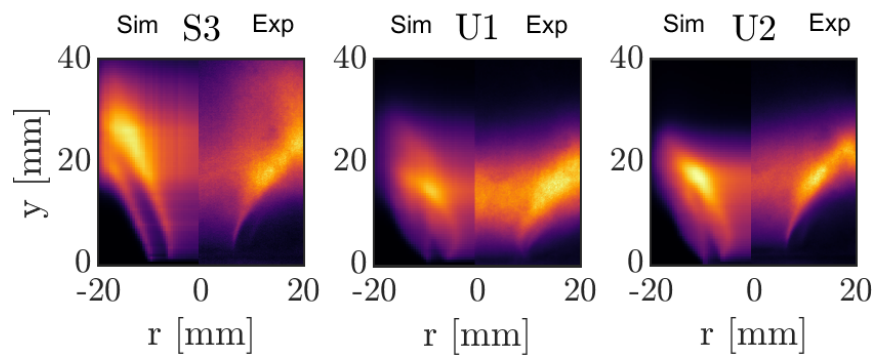Figure 4: Instantaneous flame sensor field of an annular cross-section.

Figure 5: The mean heat release rate indicator from LES is shown next to the mean OH*
chemiluminescence from experimental data [30].

intensity are well captured. There are however some discrepancies, one of which is that a stronger flame front is detected in the outer shear layer of the LES compared to the experiments. Despite these discrepancies, the flame lengths agree well with differences of up to 1-2 mm, as shown in Table 2.

Figure 6 compares the p' and SPL of the LESs of Case S1 and S3 against experimental pressure traces. The Sound Pressure Level (SPL) was calculated as

$$\text{SPL} = 10 \log_{10}\left(\frac{PSD}{p_{ref}^2}\right), \tag{8}$$

where PSD is the power spectral density of the pressure fluctuations, p', and $p_{ref} = 2 \times 10^{-5}$ Pa is the reference pressure for the threshold of human hearing. The power spectral density was calculated using the periodogram method with a Hann window.

The pressure traces are taken once a steady state has been achieved. The p' of the S1 LES has approximately similar magnitudes to the experiment, but the amplitude of p' in LES is approximately double that amplitude in experiments for Case S3. The SPL plots show that much of the LES p' comes from a peak at $f = 1375$ Hz for Case S1 and 1336 Hz for Case S3. This peak is also found in the experiment, but LES over-predicts the peak value by ≈ 18 dB. In addition, the low-frequency peak at $f \approx 200$ Hz in the experiment is also captured by LES. There are several peaks at higher frequencies of $f \approx 5000$ Hz that are predicted by the LES which are not observed in the experiment for both Case S1 and S3. While not shown, Case S2 shows similar results to Cases S1 and S3. For all cases, the LES SPL decays at high frequencies of $f > 6000$ Hz. A similar under-prediction at
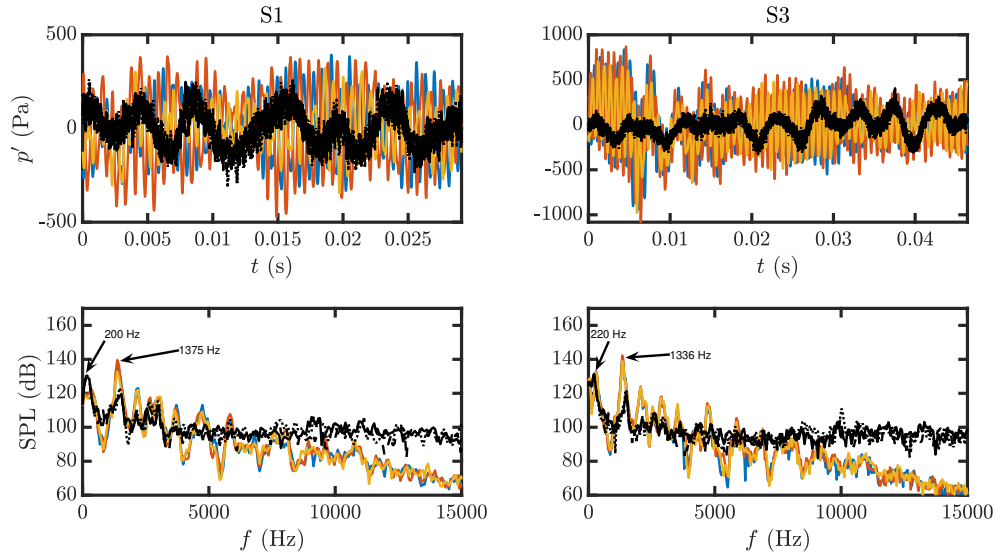
Figure 6: The top row shows the pressure traces at three points located 81 mm upstream of the injector outlet for Cases S1 and S3. The points are located in injectors 120° away from each other. The blue, red, and yellow solid lines are pressure signals from the LES, while the black solid line, black dashed line, and black dotted lines are pressure signals from the experiment [30]. The bottom row shows the SPL plots with the same legend as the top row.

high frequencies was also found in a turbulent jet LES, which is detailed in Appendix 5.1.

Figure 7 compares the p' and SPL of LES for Cases U1 and U2 against the experimental pressure traces. It is clear that a strong azimuthal pressure mode has developed in the LES. The amplitude of p' for LES is slightly overpredicted compared to the experiment in Case U1. The frequency content of the pressure signals shows that the frequency peaks of these azimuthal modes agree well with the experiments for Case U1, though it drifts further towards higher frequencies for higher order harmonics. The amplitude of

19

the fundamental frequency, second harmonic and third harmonic are over-predicted by $\approx 3 - 7$ dB, and these are the largest SPL harmonics, which explains the larger amplitudes in p'. Similar to Case U1, LES is able to reproduce the frequency of the first and second harmonic well for Case U2. However, LES strongly over-predicts the SPL of the fundamental frequency by ≈ 7 dB and the second harmonic by ≈ 26 dB. In addition, it shows a third and fourth harmonic which were not found in the experiments. This amplification of the fundamental and harmonic frequencies is responsible for the much larger p' compared to experiments.

The effect of mesh size in the flame region was also investigated in this study. Two additional LESs were run for Case U1, one with twice the Δ_x, and the other with half the Δ_x in the flame zone. It was found that a coarser mesh would require a smaller time step than 5×10^{-6} s with the second-order implicit numerical scheme to ensure the numerical scheme is not too dissipative. Interestingly, the finer mesh case requires more dissipation to wash out the pressure waves generated due to initialisation. This could not be achieved by the scheme used on the original mesh and increasing the time step to be significantly larger than 10×10^{-6} s for the first-order PISO scheme to increase the dissipative nature of the numerical scheme caused the simulation to become unstable. The flame was thickened to 6 points per mesh and this was found to increase the damping sufficiently to remove the spurious initial pressure waves. The effect of the different mesh sizes on the evolution of the solution is given in Appendix 5.2. This demonstrates that the parameters related to numerical dissipation, which in these cases are the time step and flame thickening factor, should be carefully selected to obtain
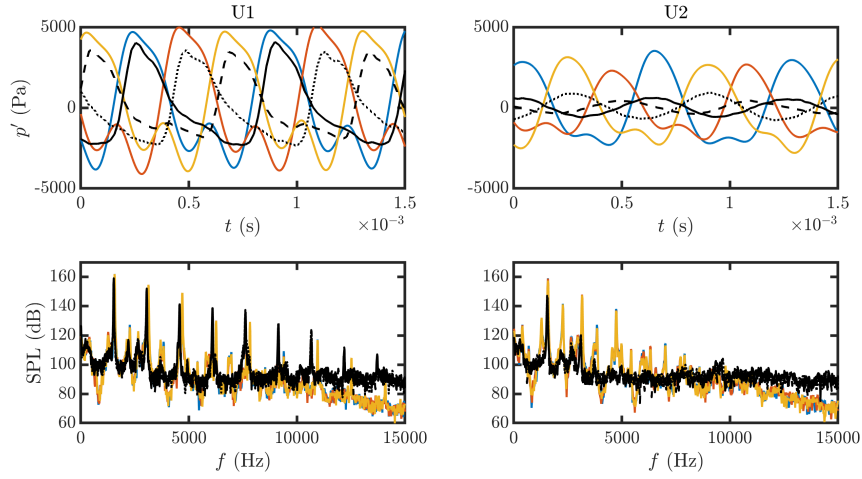
Figure 7: The top row shows the pressure traces at three points located 81 mm upstream of the injector outlet for Cases U1 and U2. The points are located in injectors 120° away from each other. The blue, red, and yellow solid lines are pressure signals from the LES, while the black solid line, black dashed line, and black dotted lines are pressure signals from the experiment [30]. The bottom row shows the SPL plots with the same legend as the top row.

the desired level of dissipation.

To further investigate the azimuthal combustion instabilities, two post-processing techniques are used, namely the quarternion representation and Dynamic Mode Decomposition (DMD). The quarternion representation will decompose the pressure waves at a certain frequency into spinning and standing components, while DMD will allow visualisation of the azimuthal modes in the combustor. The quarternion representation of the fluctuating pressure field in an annulus is employed following Ghirardo and Bothien [47]

$$p'(\Theta, t) = A\cos(n(\Theta - \theta))\cos(\chi)\cos(\omega t + \varphi) \tag{9}$$
$$+ A\sin(n(\Theta - \theta))\sin(\chi)\sin(\omega t + \varphi),$$

where Θ is the azimuthal coordinate, n describes the order of the mode, where $n = 1$ is the fundamental frequency, A is the amplitude of the mode, χ is the nature angle that indicates whether the azimuthal mode is a standing wave where $\chi = 0$, purely ClockWise (CW) spinning where $\chi = -\pi/4$, or purely CounterClockWise (CCW) spinning where $\chi = \pi/4$, θ is the angular location of the antinodal line of the standing component of the mode and is bounded in the range $[0, \pi/n]$, and φ describes the temporal phase which is related to slow and small changes of frequency. The calculation of the quarternion is implemented following Indlekofer et $al.$ [7]. For the simulations the data from all 12 injectors are used to calculate the quarternions, while for the experiments 3 pressure probes are used.

Figure 8 compares the A and χ as a function of time between the LES and experiments for Cases U1 and U2. It is noted that the direction of travel of the LES spinning modes are different for Cases U1 and U2. The LES azimuthal modes of Case U1 are spinning in the CCW direction, opposite to that of the experiment. However, in the experiment, CCW spinning modes were found for conditions that were close to the boundary of the stability envelope. Case U1 is very close to this boundary found in the experiment, and changing ϕ from 0.8 to 0.75 will result in a CCW spinning mode in the experiment. In contrast, Case U2 is far from the stability envelope and the LES correctly captures the spinning direction. It is possible that the fact that Case U1 is close to the stability envelope boundary in ϕ space causes

the LES to incorrectly predict the experimental spinning direction. Figure 8 also clearly show that LES over-predicts A, which agrees with the results of the SPL plots of Figure 7.

For both Cases U1 and U2, $\theta_{n=1}$ was found to slowly vary between $[0, \pi/n]$ and does not consistently oscillate around a mean value, which is in contrast to the experimental values of $\theta_{n=1}$ which vary by $\approx \pm 0.2°$ around a fixed mean value. For $\theta_{n=2}$, a similar result is found for Case U1 but not Case U2, where the experiment's standing mode also does not lock onto a fixed value, though the experiment's $A_{n=2}$ for this case is much smaller than LES. The fact that the LES standing modes does not lock onto a fixed θ value is surprising because there is evidence that the standing modes prefer to lock onto a location in between the injectors [48]. However, it was experimentally observed that the standing mode has transitioning periods where it deviates from the fixed mean value especially during the time period close to ignition, hence the relatively short period of time that the LES runs for compared to the experiment may not be sufficient for the LES to lock onto a fixed mean value. It is also possible that because the simulation has perfect discrete rotation symmetry when rotating about 30°, it is difficult for the standing mode to lock onto any single location [49].

Dynamic mode decomposition [50, 51] was used to extract the most energetic modes of the p' field. Figure 9 shows the instantaneous amplitude, normalised by its maximum value, of the top four most energetic DMD modes of a cross-section of the combustion chamber. It confirms that these modes are the azimuthal resonant frequencies of the annulus as they correspond to the first to fourth azimuthal modes. Interestingly, the four DMD modes are
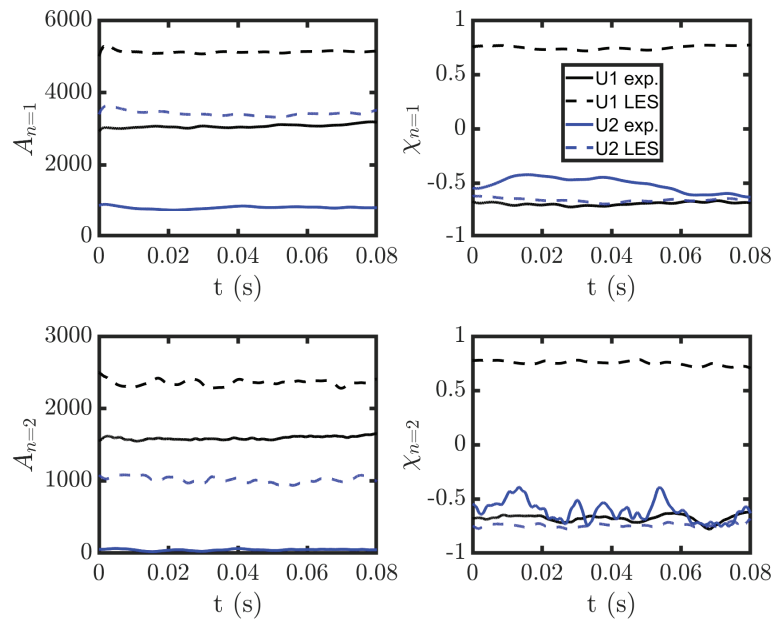
Figure 8: Amplitude, nature angle, and standing mode position of the first two azimuthal modes for Cases U1 and U2.
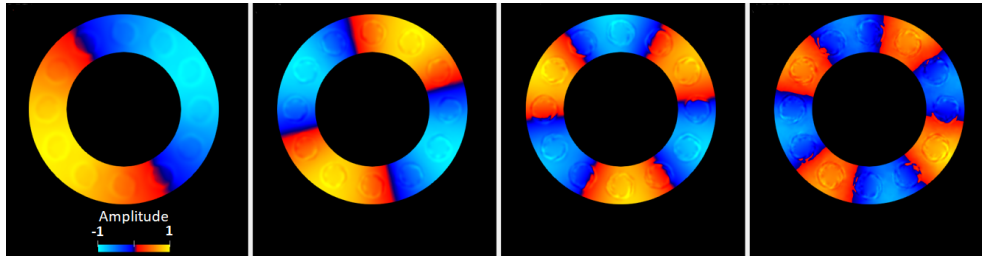
Figure 9: Instantaneous amplitude of the DMD modes of p' of Case U1, normalised by its maximum value, with the most energetic DMD mode on the left and the three following highest energy modes on the right.

not exactly in phase. This can be seen for example from the transition from positive to negative amplitude as they are not at the same location for the first two most energetic modes. This has the consequence of a small 'kink' in the pressure fluctuation for Case U1 in Figure 7, which looks like a secondary minor maxima and minima in the p' wave. This may be due to different parts of the flame driving the pressure fluctuations at different harmonic frequencies; Ahn *et al.* [32] showed that for Case U1, the transverse oscillations of the flame is in sync with the fundamental frequency and drives the pressure oscillation at this frequency, while for the first harmonic it is instead driven by asymmetric heat release rate between the left and right sides of the flame. Since these two events in the flame are different in size and location, the difference in time scales of these two events could cause a phase difference between the DMD modes of the harmonic frequencies.

Figure 10 shows the annular cross-section of the heat release rate indicator for Cases U1 and U2. For Case U1, in the negative p' half of the annulus, the flames are clearly more wrinkled and have pockets of unburnt gas close to it. At the positive p' half of the annulus, the pockets have burnt out while

the flame has become less wrinkled. Flames close to the pressure node are also found to be asymmetric around the injector axis. As an example, the flame marked with the white 'A' has significantly more wrinkling on the right side compared to its left. This asymmetry was also observed by O'Connor *et al.* [52] for standing azimuthal modes in a similar annular combustor that was not pressurised. This asymmetry was found at the pressure nodes, which have the largest velocity fluctuations [53]. Interestingly, the wrinkling and formation of flame pockets is less pronounced in Case U2, which may contribute to why Case U2 has a lower amplitude limit cycle compared to Case U1 despite having a larger s_L and hence is expected to generate larger amplitude sound waves [54, 55]. However, it is important to note that flame annihilation and the magnitude of sound generated by the flame are not the only factors that govern the amplitude of the limit cycle. The phase difference between the fluctuations of $\dot{Q}$ and p' can also significantly affect the limit cycle. Cases with smaller phase differences can cause larger limit cycle amplitudes since the forcing mechanism are more in sync with the pressure waves [32].

4. Conclusions

The capability of LES-FGM framework in capturing azimuthal modes in an intermediate pressurised annular combustor was assessed. Five cases were simulated, with three cases featuring stable combustion while the other two combustion instability was present. The same mesh size, timesteps, and numerical time discretisation scheme were used for all cases. The excited frequencies were well captured for Case U1, while the first two harmonics were
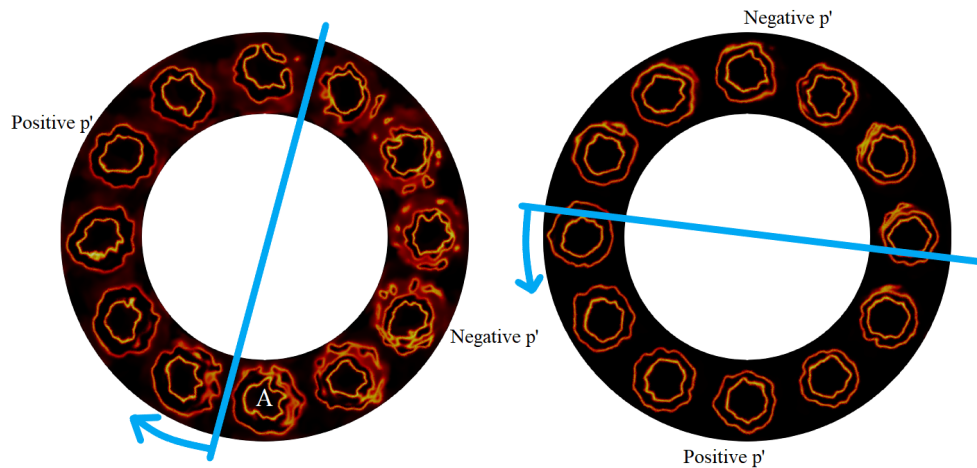
Figure 10: Annular cross-section showing the instantaneous heat release rate indicator for Case U1 (left) and U2 (right). The blue line shows the location of the node of the fundamental frequency, and the blue arrow shows the direction of travel of the azimuthal mode.

well captured for Case U2 but higher harmonics were found in the LES which were not detected in the experiment. These excited frequencies had over-predicted pressure fluctuation magnitudes, while at high frequencies of $St > 2$ LES under-predicted the pressure fluctuation magnitude. The azimuthal nature of the modes were captured well for Case U2, while Case U1 spins in the opposite direction compared to experiments. This inconsistency is likely a consequence of this case being close to the stability envelope boundary of the experiment where CCW spinning modes are found. In terms of the flame structure for the unstable cases, flames in the region of negative p' region exhibited more wrinkling and more flame pockets, while the flames in the positive p' region were less wrinkled with no flame pockets. These flame pockets and wrinkles were found to be generated and annihilated at

the same frequency as the fundamental frequency of the azimuthal mode thereby driving the instability.

Although a careful treatment of the numerical settings was needed depending on the mesh size, the core idea of the methodology was found to be useful in capturing the azimuthal modes. That is (1) initiate the solution with RANS, (2) dissipate the initial numerical waves with an LES with a large Δt and a dissipative time discretisation scheme, and (3) reduce the timestep and use a less dissipative time discretisation scheme to enable the thermoacoustic modes to develop and grow. This treatment was able to consistently capture stable and unstable modes of operation. Simulating different cases with differing levels of hydrogen addition, while keeping the simulation methodology the same, allowed the effects of hydrogen addition to flame stability to be clearly assessed with reduced uncertainty related to simulation choice differences. Future work will focus on assessing this method for higher hydrogen percentages in the mixture and also developing better combustion models for capturing the pressure fluctuations in the higher frequency range.

Acknowledgments

References

[1] T. Boushaki, Y. Dhué, L. Selle, B. Ferret, T. Poinsot, Effects of hydrogen and steam addition on laminar burning velocity of methane-air premixed

flame: Experimental and numerical analysis, Int. J. Hydrog. Energy 37 (2012) 9412–9422.

[2] J. Z. Ho, M. Talei, R. L. Gordon, M. J. Brear, Reduced chemistry for sound generation by planar annihilation in premixed methane/hydrogen flames, Proc. Combust. Inst. (2020).

[3] G. Yu, C. K. Law, C. K. Wu, Laminar flame speeds of hydrocarbon + air mixtures with hydrogen addition, Combust. Flame 63 (1986) 339–347.

[4] R. T. Hermanns, Laminar Burning Velocities of Methane-Hydrogen-Air Mixtures, Ph.D. thesis, Technische Universiteit Eindhoven, 2007.

[5] M. Fairweather, M. P. Ormsby, C. G. W. Sheppard, R. Woolley, Turbulent burning rates of methane and methane-hydrogen mixtures, Combust. Flame 156 (2009) 780–790.

[6] J. Zhang, A. Ratner, Experimental study on the excitation of thermoacoustic instability of hydrogen-methane/air premixed flames under atmospheric and elevated pressure conditions, Int. J. Hydrog. Energy 44 (2019) 21324–21335.

[7] T. Indlekofer, A. Faure-Beaulieu, N. Noiray, J. Dawson, The effect of dynamic operating conditions on the thermoacoustic response of hydrogen rich flames in an annular combustor, Combust. Flame 223 (2021) 284–294.

[8] T. C. Lieuwen, V. Yang, Combustion instabilities in gas turbine engines : (operational experience, fundamental mechanisms and modeling), AIAA, 2005.

[9] T. Poinsot, Prediction and control of combustion instabilities in real engines, Proc. Combust. Inst. 36 (2017) 1–28.

[10] A. P. Dowling, Nonlinear self-excited oscillations of a ducted flame, J. Fluid Mech. 346 (1997) 271–290.

[11] A. P. Dowling, A kinematic model of a ducted flame, J. Fluid Mech. 394 (1999) 51–72.

[12] J. O'Connor, Understanding the role of flow dynamics in thermoacoustic combustion instability, Proceedings of the Combustion Institute (2022).

[13] M. Bauerheim, F. Nicoud, T. Poinsot, Progress in analytical methods to predict and control azimuthal combustion instability modes in annular chambers, Phys. Fluids 28 (2016).

[14] L. Crocco, Aspects of combustion stability in liquid propellant rocket motors part1: Fundamentals. low frequency instability with monopropellants, J. of American Rocket Society 8 (1951) 163–178.

[15] C. Sensiau, F. Nicoud, T. Poinsot, P. Thierry, C. Sensiau, F. Nicoud, T. Poinsot, A tool to study azimuthal standing and spinning modes in annular combustors a tool to study azimuthal standing and spin-ning modes in annular a tool to study azimuthal standing and spinning modes in annular combustors, combustors. International Journal of Aeroacoustics 8 (2009) 57–67.

[16] G. Staffelbach, L. Y. Gicquel, G. Boudier, T. Poinsot, Large eddy simulation of self excited azimuthal modes in annular combustors, Proc. Combust. Inst. 32 II (2009) 2909–2916.

[17] S. Puggelli, T. Lancien, K. Prieur, D. Durox, S. Candel, R. Vicquelin, Impact of wall temperature in large eddy simulation of light-round in an annular liquid fueled combustor and assessment of wall models, J. Eng. Gas Turbine Power 142 (2020).

[18] S. Hermeth, G. Staffelbach, L. Gicquel, T. Poinsot, T. P. Les, Les evaluation of the effects of equivalence ratio fluctuations on the dynamic flame response in a real gas turbine combustion chamber, Proc. Combust. Inst. 34 (2013) 3165–3173.

[19] S. Hermeth, G. Staffelbach, L. Y. Gicquel, V. Anisimov, C. Cirigliano, T. Poinsot, Bistable swirled flames and influence on flame transfer functions, Combust. Flame 161 (2014) 184–196.

[20] M. Bauerheim, T. Jaravel, L. Esclapez, E. Riber, L. Y. M. Gicquel, B. Cuenot, M. Cazalens, S. Bourgois, M. Rullaud, Multiphase flow large-eddy simulation study of the fuel split effects on combustion instabilities in an ultra-low-nox annular combustor, J. Eng. Gas Turbine Power 138 (2015).

[21] P. Wolf, G. Staffelbach, L. Y. Gicquel, J.-D. Müller, T. Poinsot, Acoustic and large eddy simulation studies of azimuthal modes in annular combustion chambers, Combust. Flame (2013).

[22] P. Wolf, G. Staffelbach, A. Roux, L. Gicquel, T. Poinsot, V. Moureau, Massively parallel les of azimuthal thermo-acoustic instabilities in annular gas turbines, Comptes Rendus Mécanique 337 (2009) 385–394.

31

[23] P. Wolf, R. Balakrishnan, G. Staffelbach, L. Y. Gicquel, T. Poinsot, Using les to study reacting flows and instabilities in annular combustion chambers, Flow Turbul. Combust. 88 (2012) 191–206.

[24] S. Tachibana, K. Saito, T. Yamamoto, M. Makida, T. Kitano, R. Kurose, Experimental and numerical investigation of thermo-acoustic instability in a liquid-fuel aero-engine combustor at elevated pressure: Validity of large-eddy simulation of spray combustion, Combust. Flame 162 (2015) 2621–2637.

[25] N. Zettervall, N. A. Worth, M. Mazur, J. R. Dawson, C. Fureby, Large eddy simulation of CH4-air and C2H4-air combustion in a model annular gas turbine combustor, Proc. Combust. Inst. (2019) 5223–5231.

[26] J. R. Dawson, N. A. Worth, Flame dynamics and unsteady heat release rate of self-excited azimuthal modes in an annular combustor, Combust. Flame 161 (2014) 2565–2578.

[27] D. Durox, J. P. Moeck, J. F. Bourgouin, P. Morenton, M. Viallon, T. Schuller, S. Candel, Flame dynamics of a variable swirl number system and instability control, Combust. Flame 160 (2013) 1729–1742.

[28] J. F. Bourgouin, D. Durox, J. P. Moeck, T. Schuller, S. Candel, Characterization and modeling of a spinning thermoacoustic instability in an annular combustor equipped with multiple matrix injectors, J. Eng. Gas Turbine Power 137 (2015).

[29] Z. X. Chen, N. Swaminathan, M. Mazur, N. A. Worth, G. Zhang, L. Li,

Numerical investigation of azimuthal thermoacoustic instability in a gas turbine model combustor, Fuel 339 (2023) 127405.

[30] T. Indlekofer, B. Ahn, Y. H. Kwah, S. Wiseman, M. Mazur, J. R. Dawson, N. A. Worth, The effect of hydrogen addition on the amplitude and harmonic response of azimuthal instabilities in a pressurized annular combustor, Combust. Flame 228 (2021) 375–387.

[31] A. Faure-Beaulieu, T. Indlekofer, J. R. Dawson, N. Noiray, Experiments and low-order modelling of intermittent transitions between clockwise and anticlockwise spinning thermoacoustic modes in annular combustors, Proc. Combust. Inst. 38 (2021) 5943–5951.

[32] B. Ahn, T. Indlekofer, J. R. Dawson, N. A. Worth, Heat release rate response of azimuthal thermoacoustic instabilities in a pressurized annular combustor with methane/hydrogen flames, Combust. Flame 244 (2022) 112274.

[33] M. Mazur, Y. H. Kwah, T. Indlekofer, J. R. Dawson, N. A. Worth, Self-excited longitudinal and azimuthal modes in a pressurised annular combustor, Proc. Combust. Inst. 38 (2021) 5997–6004.

[34] S. D. I. Software, Simcenter star-ccm+, 2022.

[35] J. A. van Oijen, L. P. de Goey, Modelling of premixed laminar flames using flamelet-generated manifolds, Combust. Sci. Technol. 161 (2000) 113–137.

[36] J. A. van Oijen, L. P. de Goey, Modelling of premixed counterflow flames

using the flamelet-generated manifold method, Combust. Theory Model. 6 (2002) 463–478.

[37] O. Colin, F. Ducros, D. Veynante, T. Poinsot, A thickened flame model for large eddy simulations of turbulent premixed combustion, Phys. Fluids 12 (2000) 1843–1863.

[38] A. Scholtissek, P. Domingo, L. Vervisch, C. Hasse, A self-contained progress variable space solution method for thermochemical variables and flame speed in freely-propagating premixed flamelets, Proc. Combust. Inst. 37 (2019) 1529–1536.

[39] J. O. Hirschfelder, C. F. Curtiss, R. B. Bird, Molecular theory of gases and liquids, Wiley, 1964.

[40] A. Donini, R. J. Bastiaans, J. A. van Oijen, L. H. P. de Goey, The implementation of five-dimensional fgm combustion model for the simulation of a gas turbine model combustor, Turbo Expo: Power for Land, Sea and Air 56680 (2015).

[41] F. Charlette, C. Meneveau, D. Veynante, A power-law flame wrinkling model for les of premixed turbulent combustion part i: Non-dynamic formulation and initial tests, Combust. Flame 131 (2002) 159–180.

[42] S. Jella, G. Bourque, P. Gauthier, P. Versailles, J. Bergthorson, J. W. Park, T. Lu, S. Panigrahy, H. Curran, Analysis of auto-ignition chemistry in aeroderivative premixers at engine conditions, J. Eng. Gas Turbine Power 143 (2021).

[43] T. J. Poinsot, S. K. Lele, Boundary conditions for direct simulations of compressible viscous flows, J. Comput. Phys. 101 (1992) 104–129.

[44] W. K. Metcalfe, S. M. Burke, S. S. Ahmed, H. J. Curran, A hierarchical and comparative kinetic modeling study of C1 - C2 hydrocarbon and oxygenated fuels, Int. J. Chem. Kinet. 45 (2013) 638–675.

[45] C. Ji, D. Wang, J. Yang, S. Wang, A comprehensive study of light hydrocarbon mechanisms performance in predicting methane/hydrogen/air laminar burning velocities, Int. J. Hydrog. Energy 42 (2017) 17260–17274.

[46] F. Nicoud, F. Ducros, Subgrid-scale stress modelling based on the square of the velocity gradient tensor, Flow Turbul. Combust. 62 (1999) 183–200.

[47] G. Ghirardo, M. R. Bothien, Quaternion structure of azimuthal instabilities, Phys. Rev. Fluids 3 (2018) 1–23.

[48] G. Ghirardo, M. P. Juniper, J. P. Moeck, Weakly nonlinear analysis of thermoacoustic instabilities in annular combustors, J. Fluid Mech. 805 (2016) 52–87.

[49] T. Indlekofer, A. Faure-Beaulieu, J. R. Dawson, N. Noiray, Spontaneous and explicit symmetry breaking of thermoacoustic eigenmodes in imperfect annular geometries, J. Fluid Mech. 944 (2022).

[50] P. J. Schmid, Dynamic mode decomposition of numerical and experimental data, J. Fluid Mech. 656 (2010) 5–28.

[51] N. Demo, M. Tezzele, G. Rozza, Pydmd: Python dynamic mode decomposition, J. Open Source Softw. 3 (2018) 530.

[52] J. O'Connor, N. A. Worth, J. R. Dawson, Flame and flow dynamics of a self-excited, standing wave circumferential instability in a model annular gas turbine combustor, Proceedings of the ASME Turbo Expo (2013) 1–15.

[53] K. Prieur, D. Durox, T. Schuller, S. Candel, Strong azimuthal combustion instabilities in a spray annular chamber with intermittent partial blow-off, J. Eng. Gas Turbine Power 140 (2018).

[54] W. C. Strahle, Combustion Generated Noise in Turbopropulsion Systems, Technical Report, Georgia Institute of Technology, 1972.

[55] M. Talei, M. J. Brear, E. R. Hawkes, Sound generation by laminar premixed flame annihilation, J. Fluid Mech. 679 (2011) 194–218.

[56] D. Brouzet, M. Talei, M. J. Brear, B. Cuenot, The impact of chemical modelling on turbulent premixed flame acoustics, J. Fluid Mech. 915 (2021) 1–33.

[57] N. Jarrin, S. Benhamadouche, D. Laurence, R. Prosser, A synthetic-eddy-method for generating inflow conditions for large-eddy simulations, Int. J. Heat Fluid Flow 27 (2005) 585–593.

[58] J. Smagorinsky, General circulation experiments with the primitive equations: I. the basic experiment., Mon. Weather Rev. 91 (1963) 99–164.

[59] M. Germano, U. Piomelli, P. Moin, W. H. Cabot, A dynamic subgrid-scale eddy viscosity model, Proc. Summer Program, Cent. for Turb. Research (1991) 1760–1765.

[60] D. K. Lilly, A proposed modification of the Germano subgrid-scale closure method, Phys. Fluids A 4 (1992) 633–635.

[61] T. P. Coffee, Kinetic mechanisms for premixed, laminar, steady state methane/air flames, Combust. Flame 55 (1984) 161–170.

[62] X. Wu, P. Moin, A direct numerical simulation study on the mean velocity characteristics in turbulent pipe flow, J. Fluid Mech. 608 (2008) 81–112.

[63] L. Y. M. Gicquel, G. Staffelbach, T. Poinsot, P. Thierry, Large eddy simulations of gaseous flames in gas turbine combustion chambers, Prog. Energy Combust. Sci 38 (2012).

[64] I. Langella, N. A. Doan, N. Swaminathan, S. B. Pope, Study of subgrid-scale velocity models for reacting and nonreacting flows, Phys. Rev. Fluids 3 (2018).

[65] M. C. Ma, M. Talei, R. D. Sandberg, Direct numerical simulation of turbulent premixed jet flames: Influence of inflow boundary conditions, Combust. Flame 213 (2020) 240–254.

[66] I. R. Hurle, R. B. Price, T. M. Sugden, A. Thomas, Sound emission from open turbulent premixed flames, Proc. Math. Phys. Eng. Sci. 303 (1968) 409–427.

[67] R. Rajaram, T. Lieuwen, Acoustic radiation from turbulent premixed flames, J. Fluid Mech. 637 (2009) 357–385.

[68] D. Brouzet, Investigation of Direct Combustion Noise in Turbulent Premixed Jet Flames Using Direct Numerical Simulations, Ph.D. thesis, The University of Melbourne, 2020.

[69] P. Panek, D. Brouzet, M. Talei, R. L. Gordon, A priori assessment of flame surface density modelling for large-eddy simulation of sound generation by turbulent premixed flames, Combust. Flame 241 (2022).

5. Appendix

5.1. Turbulent jet case

This appendix provides the details of the turbulent jet case run to investigate how well the LES-FGM framework captures combustion noise. The Direct Numerical Simulation (DNS) dataset of a turbulent jet flame generating sound will be used [56]. The effect of LES-FGM on the sound generated by an open flame will be compared against this DNS dataset.

The details of the DNS can be found in the paper by Brouzet *et al.* [56], and only relevant parameters for this work are shown in Table 3. The variables in the table are the pressure, p, the equivalence ratio, ϕ, the inlet pipe diameter, D, the unstretched laminar flame speed, s_L, the Karlovitz number, Ka, and Damköhler number, Da, the streamwise length, L_x, and the two spanwise lengths, L_y and L_z. The bulk Reynolds number is defined as $\mathrm{Re_D} = u_{in}D/\nu$, where u_{in} is the mean bulk velocity, and ν is the kinematic viscosity.

Table 3: Flow and flame parameters for the turbulent jet.

Parameter	Value
T_u [K]	700
p [atm]	1.0
ϕ	1.0
D [mm]	1.85
Domain size $(L_x \times L_y \times L_z)$	$20D \times 16D \times 16D$
s_L [m/s]	2.03
δ_{th} [μm]	313
$\mathrm{Re_D}$	5800
Ka	15.4
Da	0.50

To ensure that the inlet turbulence to the flame is correctly generated, the inlet pipe was simulated in the LES (see Figure 11). As such, the domain was made of two sections. The first is a rectangular chamber with dimensions $20D \times 16D \times 16D$ and the second section is a $100D$ pipe with adiabatic walls. The pipe's outlet serves as the inlet to the rectangular combustion domain. The inlet of the pipe is a mass flow inlet and turbulence is initialised using the synthetic eddy method [57] and allowed to develop in the $100D$ pipe. The outlet conditions were set as non-reflecting pressure outlet with Local One-Dimensional Inviscid (LODI) assumptions [43]. The dynamic Smagorinsky subgrid scale model [58–60] was used with the model constant related to the timescales, $C_t = 2.5$, where C_t is used to calculate the subgrid scale turbulent kinetic energy, k_{SGS} as
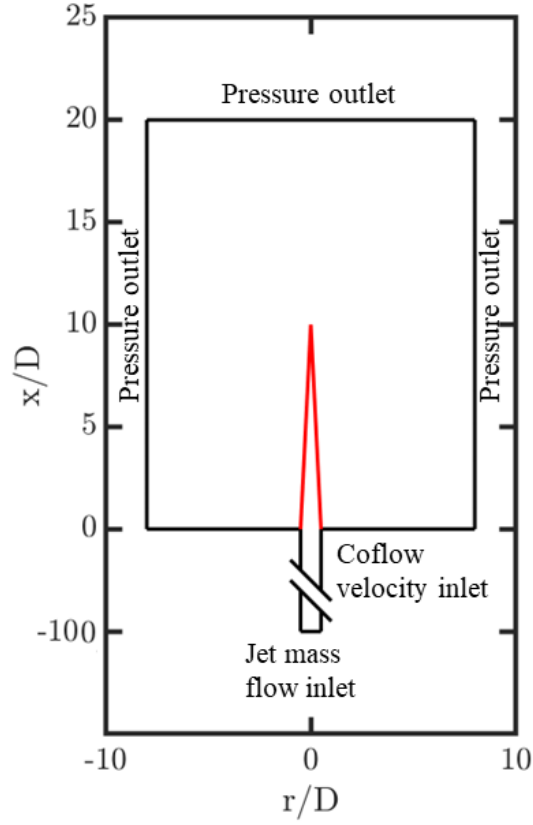
Figure 11: Computational domain of the jet flame. A sketch of the flame is shown in the red lines.

$$k_{SGS} = C_t \frac{\mu_t}{\rho} S, \tag{10}$$

where μ_t is the turbulent viscosity, and S is the norm of the mean strain rate tensor computed from the resolved velocity field.

A 14-species methane chemistry mechanism [61] (details are provided in the appendix of Brouzet *et al.* [56]) which is the same as that used in the DNS study, was used to generate the FPF flamelet for LES-FGM. A trimmed cell mesher was used to generate the mesh and the mesh size in the combusting

Table 4: Turbulent jet cases.

Case	Δ_x/δ_{th}	Number of prism layers	$\mathbf{CFL_{ac}}$
1	0.5	11	0.5
2	0.5	0	0.5
3	0.5	11	1.0
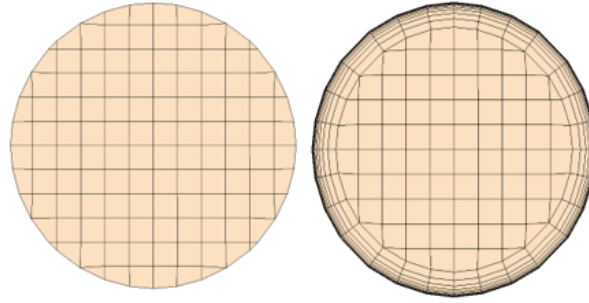
Figure 12: Pipe mesh with $\Delta_x = 0.5\delta_{th}$ with (right) and without (left) prism layers.

region was set to be $1\delta_{th}$.

Three cases with different grid layouts and timesteps were simulated. Table 4 shows the cases with different grid sizes, Δ_x, in the pipe, number of prism layers, and Courant-Friedrichs-Lewy (CFL) number based on sound speed, $\mathrm{CFL_{ac}}$. Case 1 is the base case and will be compared against the rest. The prism layers are defined such that the grid size closest to the wall, $\Delta_x^+ < 1$, where $\Delta_x^+ = (\Delta_x \rho u_\tau)/\mu$, ρ is the fluid density, and μ is the dynamic viscosity. The friction velocity, $u_\tau = \sqrt{\frac{\tau_w}{\rho}}$, is found using the wall shear stress $\tau_w = \rho\mu(\frac{du_k}{dy}|_{y=0})$, where μ is the dynamic viscosity, ρ is the density, u_k is the streamwise velocity, and y is the wall normal coordinate. Case 2 does not have prism layers. Figure 12 shows the pipe mesh for Cases 1 and 2. Case 3 has a larger $\mathrm{CFL_{ac}}$ compared to Case 1.
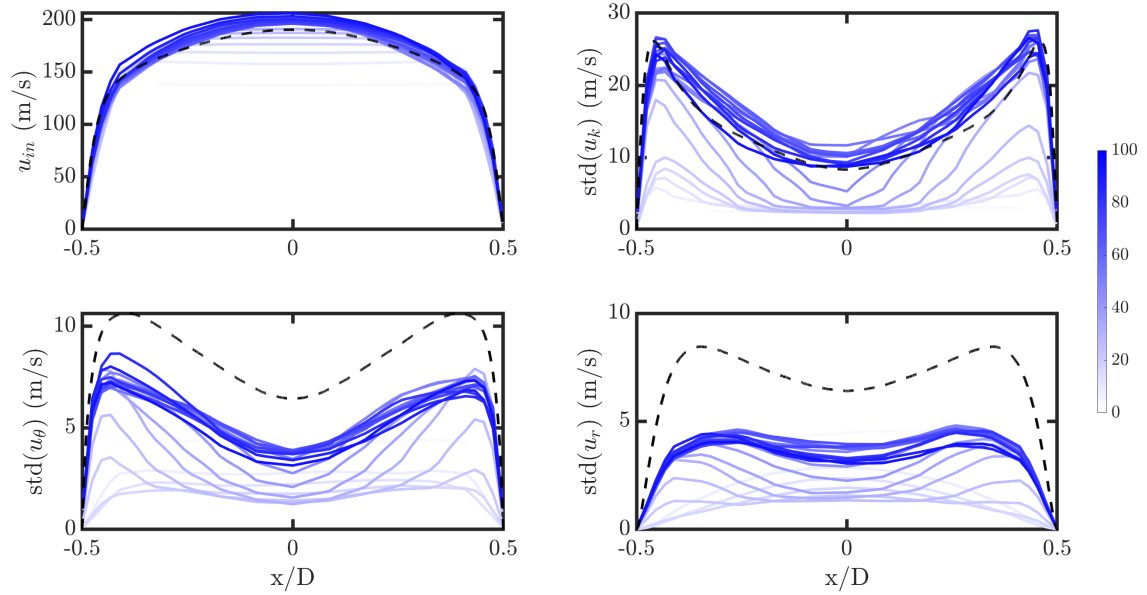
Figure 13: u_{in}, $\text{std}(u_k)$, $\text{std}(u_\theta)$, and $\text{std}(u_r)$ for Case 1 are shown in the blue lines. The blue lines are the profiles at distances spaced $x/D = 5$ apart, with darker lines closer to the outlet of the $100D$ pipe. The dashed black line denotes the profile from experiment [62].

To accurately simulate the flame in LES, the inlet turbulence needs to be consistent with that in the DNS. Figure 13 shows the mean streamwise velocity, standard deviation of the streamwise velocity, $\text{std}(u_k)$, standard deviation of the azimuthal velocity, $\text{std}(u_\theta)$, and standard deviation of the radial velocity, $\text{std}(u_r)$, for Case 1. It shows that while u_{in} and $\text{std}(u_k)$ profiles are well captured, the $\text{std}(u_\theta)$ and $\text{std}(u_r)$ appear to be under-predicted. However, this analysis only takes into account the resolved velocity fluctuations.

For a full picture of how well turbulence is captured, the total turbulent kinetic energy, k, including both unresolved and resolved scales, is evaluated. Figure 14 shows the maximum k in the pipe as the turbulence develops over
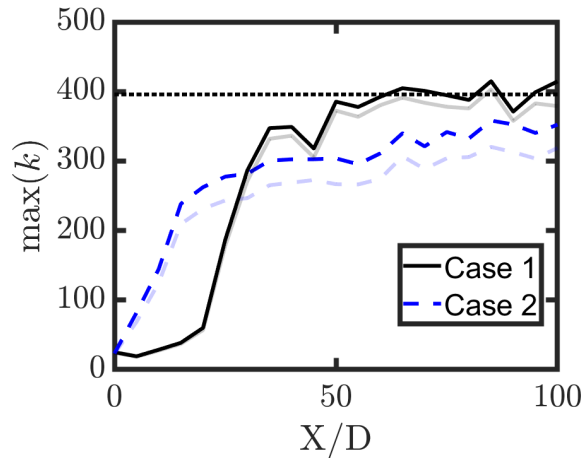
42

Figure 14: The solid line shows the maximum total turbulent kinetic energy along the pipe for Case 1 and Case 2. The transparent lines show only the resolved component of k. The dotted horizontal line shows the maximum turbulent kinetic energy from the turbulent pipe flow profile of [62].

the $100D$ pipe for Cases 1 and 2. The maximum of k at a given streamwise location is defined as the maxima of k over the radius of the pipe at that streamwise location. The total turbulent kinetic energy converges towards its maximum reported for the turbulent pipe flow profile of [62] for Case 1, though the absence of prism layers cause Case 2 to under-predict k. For Case 1, most of the k is resolved due to the presence of the prism layers which resolve the near wall turbulence development in the pipe. However, for Case 2 there is a significant contribution from the subgrid scales, hence we rely on the subgrid scale model to capture the unresolved component of k.

Figure 15 shows the comparison of k for the WALE and dynamic Smagorinsky subgrid scale models for only the turbulent pipe. WALE performs similarly compared to the dynamic Smagorinsky subgrid scale model after $100D$,
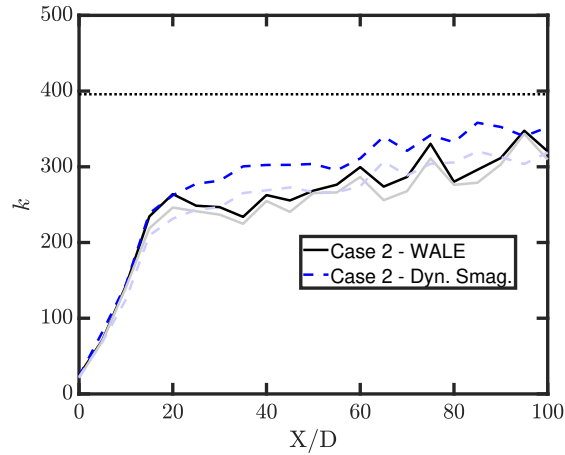
Figure 15: The solid line shows the maximum total turbulent kinetic energy along the pipe for Case 2. The transparent lines show only the resolved component of k. The dotted horizontal line shows the maximum turbulent kinetic energy from the turbulent pipe flow profile of [62].

though it takes longer to reach a similar level of k as the dynamic Smagorinsky model case.

A flame length based on the temperature field, $L_{f,T}$, was defined as the distance between the injector tip and 50% of the adiabatic flame temperature at the centreline. Figure 16 shows the mean temperature for the DNS results, Case 1 and Case 2, and the measured flame lengths are also shown in Table 5. It can be seen that LES over-predicts $L_{f,T}$. This over-prediction is possibly a result of the over-prediction of turbulent and numerical diffusivity by the eddy viscosity model which has been found to be significant when there is strong mean shear [63]. This leads to artificial re-laminarisation of the flame and can extend the flame length. In addition, despite simulating the $100\ D$ pipe and achieving similar total kinetic energy between DNS and

44

LES, the inlet turbulent profiles may still be inconsistent with DNS. There are several reasons that may contribute to this inconsistency. Firstly, the Smagorinsky subgrid scale model has been shown to predict inconsistent values of k compared to DNS data [64], which may significantly affect the $\text{std}(u_r)$ and $\text{std}(u_\theta)$ profiles since they rely on the subgrid scales significantly as shown in Figure 13. Secondly, the turbulence used in the inlet of the DNS was initialised from homogeneous isotropic turbulence that was then modified to fit experimental turbulence profiles. This differs from the the LES which simulated a 100 D pipe, and it has been shown that simulating a pipe as opposed to initialising the inlet with synthetic turbulence can lead to different flame lengths [65].

Table 5 also shows the flame length defined as the distance from 10% to 90% of the radially integrated variance of heat release rate $L_{f,\text{var}(\dot{Q})}$ [56]. This variable was used as a measure of flame length in the DNS study [56] since the $\text{var}(\dot{Q})$ can be linked to combustion noise [54, 66], and a flame length defined using the variance of heat release rate was directly related to the spectral characteristics of the sound generated by the flame [67]. Interestingly, despite the over-prediction of $L_{f,T}$, the $L_{f,\text{var}(\dot{Q})}$ is much closer to the DNS. The agreement between DNS and LES for this parameter is important because the fluctuations of $\dot{Q}$ is expected to generate significant combustion noise, and the LES sound signals are now compared against DNS.

Figure 17 shows the SPL plots of eight pressure probes at different radial and streamwise locations against the Strouhal number, $\text{St} = fD/u_{in}$, which is the frequency non-dimensionalised by the inlet velocity and inlet diameter. Pressure signals were recorded at locations $x/D = 5D, 10D, 15D, 20D$
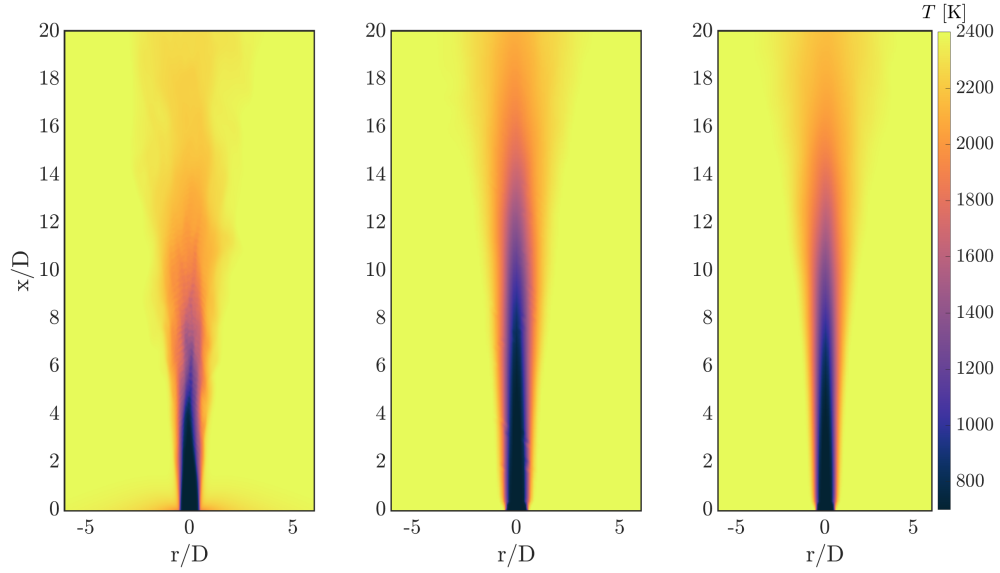
Figure 16: Mean temperature for the DNS (left), Case 1 (middle), and Case 2 (right).

Table 5: Flame lengths for the DNS [68], Case 1, and Case 2.

Flame length definition	DNS	Case 1	Case 2
$L_{f,T}/D$	5.8	10.5	9.2
$L_{f,\mathrm{var}(\dot{Q})}/D$	12.9	14.5	13.3

downstream of the pipe outlet, and $r/D = 6D, 8D$ away from the jet centre-line. The agreement for all probes for frequencies St< 1 is very good and the shape of the spectra agrees well with the DNS SPL but discrepancies appear at higher frequencies. For all probes, there is under-prediction at very high frequencies of St ≈ 10 of up to 18 dB. This under-prediction is worst for Case 3 as the CFL number is higher, hence dissipation of high frequency pressure waves is stronger. For the pressure probes located at $R = 8D$, this under-prediction at higher frequencies is more severe since the pressure waves must travel a larger distance in the coarse $\Delta_x = 2$ mm mesh. In addition, for the probes located at $x/D \geq 15$, there is over-prediction of up to 12 dB at St > 1. It can also be observed that there is a local 'peak' at St ≈ 10.5, which is not captured by any of the LES cases for all probes.It is interesting that discrepancies occur at St> 1 because for this frequency range, the sound from annihilation events were found to dominate the sound spectrum [56].

If a Strouhal number was defined using δ_{th}, St$_{\delta_{th}} = f\delta_{th}/u_{in}$, instead of D, the peak at St $= 10.5$ would occur at St$_{\delta_{th}} \approx 1.7$. The acoustic waves generated at a length scale of δ_{th} is indicative of flame-flame interaction events. This suggests that the difficulty of modelling annihilation events in the combustion model may be a possible cause for this discrepancy, which can greatly impact the sound spectra for this frequency range. This under-prediction for St> 1 was also observed in the *a priori* study of Panek *et al.* [69] who compared DNS pressure fluctuations against the pressure fluctuations predicted by flame surface density combustion models. It is also possible that the low order discretisation schemes are highly dissipative for high frequencies which could explain this discrepancy. In addition, in an LES, the flame fronts are
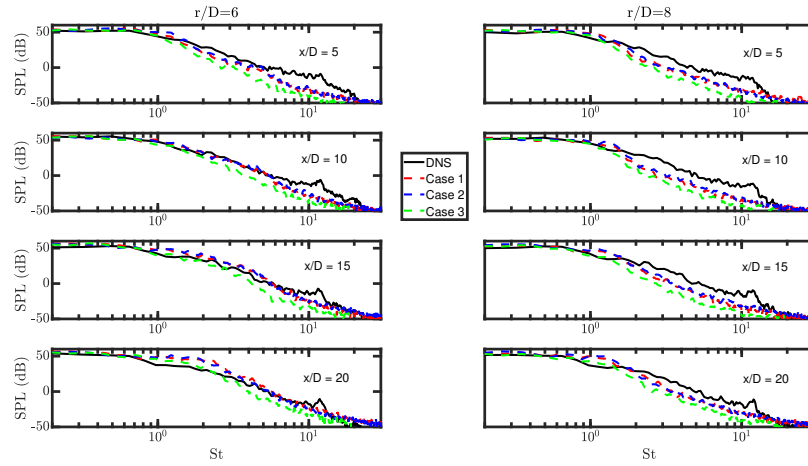
47

Figure 17: SPL of DNS in black solid line, Case 1 in red dashed line, Case 2 in blue dashed line, and Case 3 in green dashed line. The left column shows the results at a probe point $6D$ away from the jet centreline, while the right column shows the results at a probe point $8D$ away from the jet centreline. The first row shows results at probe points located $5D$ away from the pipe outlet, second row $10D$ away, third row $15D$ away, and fourth row $20D$ away.

not fully resolved which causes annihilation events to be much more rare, and this effect is further compounded by the thickened flame model. This can have a significant effect on the sound generated at high frequencies.

5.2. Mesh sensitivity analysis

The details of the mesh sensitivity analysis for Case U1 are provided in this appendix. Figure 18 shows p' for a single pressure probe for Case U1 with the base mesh of $\Delta_x = 0.7$ mm, a coarser mesh $\Delta_x = 1.4$ mm, and a finer mesh $\Delta_x = 0.35$ mm, starting from the point in time when the time discretisation scheme switches to the 2nd order implicit scheme. The $\Delta_x = 1.4$ and 0.35 mm cases develop azimuthal waves similar to what was
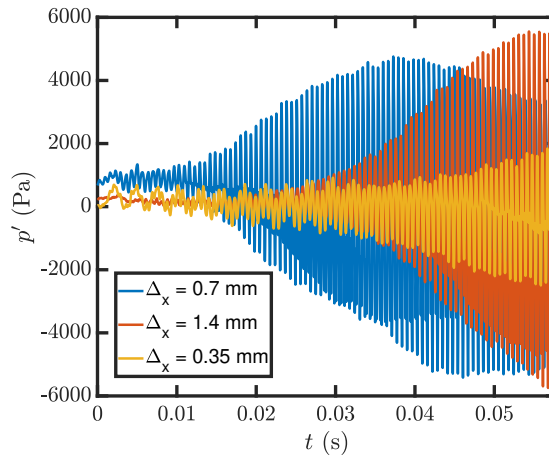
Figure 18: Pressure fluctuations of a single pressure probe for Case U1 with the base mesh $\Delta_x = 0.7$ mm, a coarser mesh $\Delta_x = 1.4$ mm, and a finer mesh $\Delta_x = 0.35$ mm. $t = 0$ denotes the time when the time discretisation scheme switches to the 2nd order implicit discretisation scheme.

found in the $\Delta_x = 0.7$ mm case, though the rate of increase in amplitude differs between each case. The $\Delta_x = 0.7$ mm case develops the fastest and achieves its limit cycle, while the $\Delta_x = 1.4$ mm case takes longer to develop the azimuthal modes, possibly due to increased dissipation at higher mesh sizes. The $\Delta = 0.35$ mm case develops these modes very quickly, though it takes far longer to achieve its limit cycle, and in fact for the simulation time of ≈ 0.06 s has not yet attained its limit cycle. The frequency content of the cases are compared next.

Only a portion of the pressure fluctuation from the $\Delta_x = 0.7$ and 1.4 mm mesh were shown in Figure 18, and this portion corresponds to the length of the simulation for the expensive $\Delta_x = 0.35$ mm case. The SPL graph for this portion of data for each case is shown in Figure 19 and pressure fluctuation
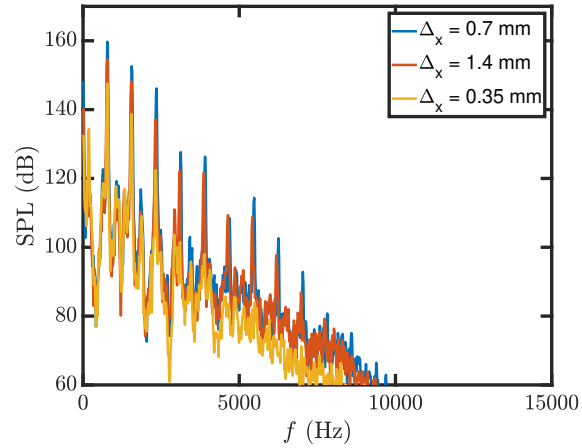
Figure 19: SPL of a single pressure probe for Case U1 with the base mesh $\Delta_x = 0.7$ mm, a coarser mesh $\Delta_x = 1.4$ mm, and a finer mesh $\Delta_x = 0.35$ mm.

of the last ≈ 2.5 ms is shown in Figure 20. These two graphs show that the spectral content of the sound are approximately the same for each of the cases as they show similar peaks and drop-off behaviour. The discrepancies in the amplitude of the peaks is likely due to the longer time it takes for the $\Delta_x = 1.4$ and 0.35 mm cases to achieve the limit cycle.
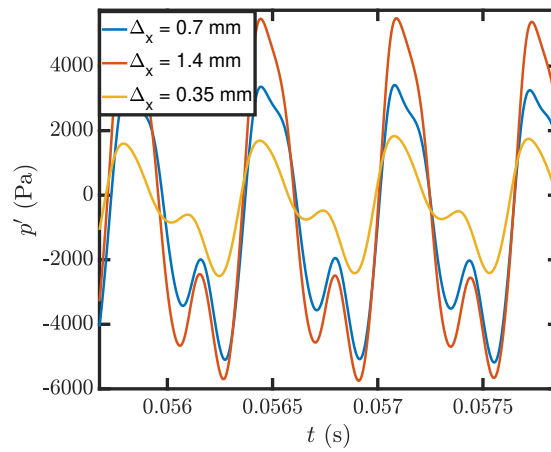
Figure 20: Last ≈ 3 wavelengths of pressure fluctuations of a single pressure probe shown in Figure 18. The pressure signals have been shifted slightly so that the maxima lie on top of each other.